

See discussions, stats, and author profiles for this publication at: <https://www.researchgate.net/publication/51713224>

Photocurrent Enhancement by Surface Plasmon Resonance of Silver Nanoparticles in Highly Porous Dye-Sensitized Solar Cells

ARTICLE *in* LANGMUIR · DECEMBER 2011

Impact Factor: 4.46 · DOI: 10.1021/la203557f · Source: PubMed

CITATIONS

70

READS

107

3 AUTHORS:



Nak Cheon Jeong

Daegu Gyeongbuk Institute of Science and T...

38 PUBLICATIONS 1,283 CITATIONS

SEE PROFILE



Chaiya Prasittichai

Kasetsart University

16 PUBLICATIONS 462 CITATIONS

SEE PROFILE



Joseph Hupp

Northwestern University

521 PUBLICATIONS 29,507 CITATIONS

SEE PROFILE

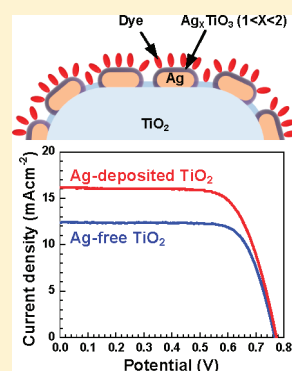
Photocurrent Enhancement by Surface Plasmon Resonance of Silver Nanoparticles in Highly Porous Dye-Sensitized Solar Cells

Nak Cheon Jeong, Chaiya Prasittichai, and Joseph T. Hupp*

Department of Chemistry and Argonne–Northwestern Solar Energy Research Center (ANSER), Northwestern University, 2145 Sheridan Road, Evanston, Illinois 60208, United States

S Supporting Information

ABSTRACT: Localized surface plasmon resonance (LSPR) by silver nanoparticles that are photochemically incorporated into an electrode-supported TiO_2 nanoparticulate framework enhances the extinction of a subsequently adsorbed dye (the ruthenium-containing molecule, N719). The enhancement arises from both an increase in the dye's effective absorption cross section and a modest increase in the framework surface area. Deployment of the silver-modified assembly as a photoanode in dye-sensitized solar cells leads to light-to-electrical energy conversion with an overall efficiency of 8.9%. This represents a 25% improvement over the performance of otherwise identical solar cells lacking corrosion-protected silver nanoparticles. As one would expect based on increased dye loading and electromagnetic field enhanced (LSPR-enhanced) absorption, the improvement is manifested chiefly as an increase in photocurrent density ascribable to improved light harvesting.



INTRODUCTION

Dye-sensitized solar cells (DSSCs) have received great attention as a promising technology for renewable energy production, in part because they can be fabricated from low-cost materials. To improve efficiencies of DSSCs, efforts have been directed at engineering the anode, cathode, dye, and redox shuttle. For instance, coating mesoporous TiO_2 networks with various types of insulating metal oxides,^{1,2} replacing TiO_2 by other semiconducting oxides,^{3,4} fabricating networks from highly porous aerogels,⁵ selectively positioning several kinds of dyes to form multicolored layers of porous networks,⁶ synthesizing new dyes that broadly and effectively absorb visible and near-infrared light,⁷ synthesizing alternative redox shuttles,⁸ and substituting the platinized dark electrode with a secondary photoelectrode have all been investigated.^{9,10} Nevertheless, the photoanode has been regarded as paramount since the factors for improving efficiency such as presenting a high density of light-harvesting molecules, fast electron injection from dyes to networks, fast electron transport within networks, slow back electron transfer to oxidized dyes and shuttles, and high open-circuit photovoltages (V_{OC}) are determined, at least in part, by the properties of the anode.

Localized surface plasmon resonance (LSPR) behavior is an intriguing characteristic of metal nanoparticles (NPs). LSPR is generated by resonance between electric fields of electromagnetic waves and free electrons in metal nanoparticles. It has been used to advantage in surface-enhanced spectroscopy,¹¹ biological and chemical imaging,^{12,13} lithographic fabrication,¹⁴ and other applications.^{15,16} One of the most intriguing features of LSPR behavior is that it can enhance the apparent extinction coefficient of molecules adsorbed on suitable metal nanoparticles.^{17,18} Based on the above, studies of the effects of LSPR on the performance of

photoelectrodes have been attempted.^{17–26} While some studies were subsequently found to be compromised by unrecognized corrosion or photocorrosion of plasmonic particles, others appear robust. In one study involving carefully corrosion-protected photoelectrodes, the extinction of the dye, N3 (i.e., $\text{Ru}(4,4'\text{-carboxylic acid-2,2'-bipyridine})_2(\text{NCS})_2$), adsorbed on nanosized Ag islands was ~ 10 times higher than that of N3 adsorbed on a bare FTO (fluorine-doped tin oxide) platform.¹⁷ This enhancement led to a sevenfold increase in overall energy conversion efficiency. However, efficiencies were still very low ($\sim 0.05\%$) owing to the extremely low surface areas of two-dimensional arrays of protected silver nanoparticles.

In this report, we have extended the investigation to high-area photoanodes to determine whether the silver-based plasmon-amplification strategy can be used to enhance the performance of DSSCs that already are operating at reasonably high efficiency. As detailed below, we find that efficiencies indeed can be improved significantly. While our report was in preparation, related reports appeared by Qi and co-workers²⁷ and by Brown and co-workers.²⁸ Their observations, based on silver and gold nanoparticles, respectively, are broadly consistent with ours.

EXPERIMENTAL SECTION

Preparation of Electrodes for Photovoltaic Studies. Samples of FTO-coated glass ($10 \text{ } \Omega \text{ cm}^{-2}$, Hartford glass) with dimensions of

Received: September 11, 2011

Revised: October 12, 2011

$15 \times 15 \text{ mm}^2$ were refluxed in 40 mM TiCl_4 in isopropyl alcohol (prepared from 90 mM TiCl_4 in 20% HCl solution, Aldrich) for 30 min and then calcined at 420°C for 30 min. For fabrication of transparent TiO_2 layers (TL), TiO_2 paste featuring 18 nm diameter particles (DSL 18NR-T, Dyesol) was deposited on the FTO samples by doctor-blading. After each film was dried, a scattering TL was deposited in similar fashion, but using TiO_2 paste featuring 400 nm diameter particles (WER4-0, Dyesol). The multilayer film was then calcined at 420°C for 30 min. For deposition of Ag NPs, 5 μL of 5 mM AgNO_3 (99.995%, Aldrich)/EtOH solution was dropcast on each film, and the sample was irradiated with UV light (mixed 254 and 365 nm wavelength, UVGL-15 compact UV lamp, UVP) for 5 min after solvent was evaporated. This step was repeated three times to optimize photovoltaic performance. Finally, composite films were refluxed in 1.0 M TIP (titanium(IV)isopropoxide, Aldrich) in isopropyl alcohol solution for 25 min and then calcined at 370°C for 15 min. For samples lacking Ag NPs, we followed the above procedure (including treatment with TIP) but omitted the dropcasting-related steps. N719 (Dyesol) was loaded onto photoelectrodes by soaking them for 24 h in a 0.5 mM solution in ethanol. Cathodes were prepared by drilling a 0.3 mm diameter hole in each of several FTO-coated glass samples. Then, 10 μL of a 5 mM solution of H_2PtCl_6 (Aldrich) in ethanol was dropcast on the FTO samples and allowed to dry. Finally, the cathodes were calcined for 30 min at 380°C .

Assembly of Photovoltaic Cells. Cathode/anode pairs were combined in each case with a 60 μm thick Surllyn polymer film (Surllyn-1702, Dupont) that served as a spacer and defined the perimeter of a photoelectrochemical sealing. The components were permanently combined by placing them on a hot plate at 170°C and allowing the spacer to melt slightly. Tin-coated copper wires were connected to each electrode with silver epoxy. 1-Butyl-3-methylimidazolium iodide (0.60 M) (98%, TCI), 0.03 M I_2 (99.8%, Aldrich), 0.10 M guanidine thiocyanate (99%, Aldrich), and 0.50 M 4-*tert*-butylpyridine (99%, Aldrich) in an 85:15 vol % mixture of acetonitrile and valeronitrile (99.5%, Aldrich) constituted the cell solvent, redox electrolyte, and inert electrolyte. Approximately 30 μL of the electrolyte-containing solution was dropcast onto the drilled hole on the back side of the platinized cathode and then drawn into the cell via application of a vacuum.

Instrumentation. Scanning electron microscopy (SEM) images were obtained using a FE-SEM (Hitachi S-4800) operated at an acceleration voltage of 10 kV after samples had been coated with ca. 3 nm of a Pt–Pd alloy. Transmission electron microscope (TEM) images were obtained using a JEOL JEM-2100F at an acceleration voltage of 200 kV. XPS spectra were recorded on an ESCAPROBE spectrometer (Omicron NanoTechnology). Binding energies of Ti (2p) and Ag (3d) electrons were calibrated to the binding energy of C (1s), 284.6 eV, as an internal standard. Visible region extinction spectra of dyes and electrodes were recorded on a Varian Cary 5000 UV–vis–NIR spectrophotometer. Photocurrent-density-to-applied-voltage (J – V) and IPCE curves of samples were obtained using a home-built setup comprising a xenon lamp, an AM 1.5 light filter, and a CHI 1202 Electrochemical Analyzer (CHI instruments). The power of filtered light was calibrated by optical power meter (OPM) to 100 mW cm^{-2} .

RESULTS AND DISCUSSION

Plasmonic Photoelectrode Assembly and Characterization. In order to incorporate plasmonic particles uniformly, we prepared them directly within the mesoporous framework of already-assembled TiO_2 networks. Ag NPs were deposited on TiO_2 networks possessing high surface areas, via photoreduction of Ag^+ from dissolved AgNO_3 .²⁹ Figure 1b, a TEM image of TiO_2 NPs that had been photolyzed in an Ag^+ solution, shows that silver NPs (with diameters ranging from 3 to 8 nm) are homogeneously distributed over the titanium dioxide. In contrast,

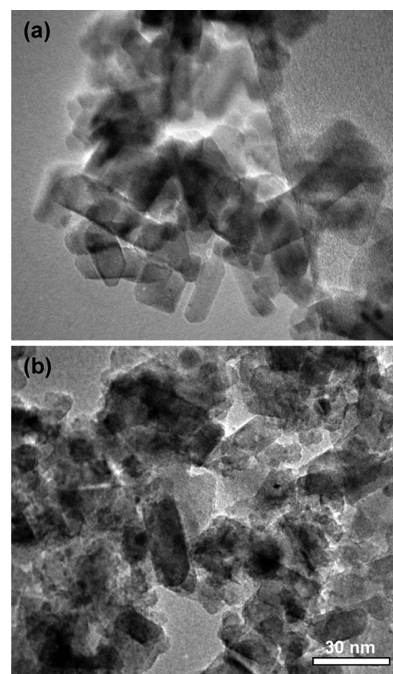


Figure 1. TEM images of TiO_2 NPs (a) and Ag NPs-deposited TiO_2 NPs (b).

metal nanoparticles are absent (as expected) from a TEM image of TiO_2 NPs that have not been exposed to Ag^+ (Figure 1a).

Silver is a reasonably stable transition metal under ambient conditions. Nevertheless, it is easily corroded when it contacts acids or strong oxidants. If strongly oxidizing tri-iodide is employed as one-half of a redox shuttle in a DSSC, any immersed Ag NPs will require protection. Previously, with particles on flat surfaces we found that atomic layer deposition (ALD) of various metal oxides could be used to create thin, pinhole-free coatings that physically isolate the particles from the surrounding corrosive electrolyte solution.^{17,23} Unfortunately, for small Ag NPs on high-area TiO_2 electrodes, we found ALD to be ineffective in preventing corrosion. Consequently, we devised instead a condensed-phase method for coating and protecting Ag NPs.

Briefly, Ag/ TiO_2 photoanodes were placed in a 1 M TIP (titanium(IV)isopropoxide) solution in refluxing isopropyl alcohol for 25 min, removed and rinsed, and then calcined at 370°C for 15 min. In the photoelectrochemical studies outlined later in our report, this protocol proved to be sufficient for preventing silver corrosion. XPS measurements were used to gauge the extent of oxidation of the silver nanoparticles. As shown in Figure 2a, the XPS spectrum in the Ag (3d) region shows two peaks; these are connected to spin–orbit coupled energy states $J = 5/2$ and $3/2$. In Ag/ TiO_2 , the Ag $3d_{5/2}$ and Ag $3d_{3/2}$ appear at 367.9 and 373.9 eV, indicating that the Ag NPs are not oxidized.³⁰ For TIP–Ag/ TiO_2 , however, both peaks are shifted to lower energy and both are broadened, with tailing extending into the higher energy regions that are characteristic of Ag^0 . The broadening points to a mix of species. We found that the Ag $3d_{5/2}$ and Ag $3d_{3/2}$ peaks each could be reasonably fit to a pair of narrower peaks, designated I and II. From the fitting, we find for I peaks at 367.4 and 373.4 eV and for II peaks at 367.9 and 373.9 eV. (Bandwidths are listed in Table S1.) The peaks designated Ag II $_{5/2}$ and Ag II $_{3/2}$ in TIP–Ag/ TiO_2 precisely match those in Ag/ TiO_2 and indicate the presence of Ag^0 . Those designated Ag I $_{5/2}$ and Ag I $_{3/2}$ are

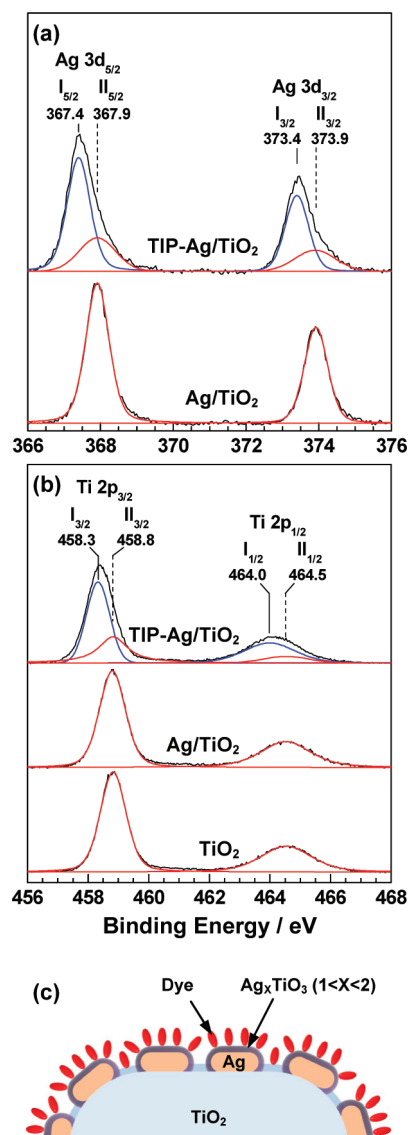


Figure 2. XPS spectra of TiO₂, Ag/TiO₂, and TIP-Ag/TiO₂ (as indicated) in the Ag (3d) region (a) and in the Ti (2p) region (b). (c) Illustration of Ag NPs deposited on TiO₂ NP.

characterized by lower binding energies and are indicative of silver oxidation. Thus both neutral and oxidized silver atoms are present. Hoflund and co-workers observed that the spin-orbit coupled binding energies of Ag 3d_{5/2} in Ag, Ag₂O, and AgO, respectively, are at 368.0, 367.7, and 367.2.³⁰ That the binding energy for silver decreases, rather than increases, as the oxidation state increases, is atypical and has been ascribed to a combination of factors, including changes in lattice potential and extra-atomic relaxation energy.³⁰ On the basis of the Hoflund work, the oxidation state of Ag here appears to be between +1 and +2 (Ag^X, and 1 < X < 2). The presence of both Ag⁰ and Ag^X is speculatively attributed to the formation of an oxidized shell around a silver nanoparticle core. The shell, presumably, is what prevents the remaining Ag⁰ from being oxidized when TIP-Ag/TiO₂ is incorporated in solar cells and exposed to tri-iodide. Finally, comparisons of XPS spectra for TIP-Ag/TiO₂ before and after calcination reveals that calcination effects little if any additional oxidation.

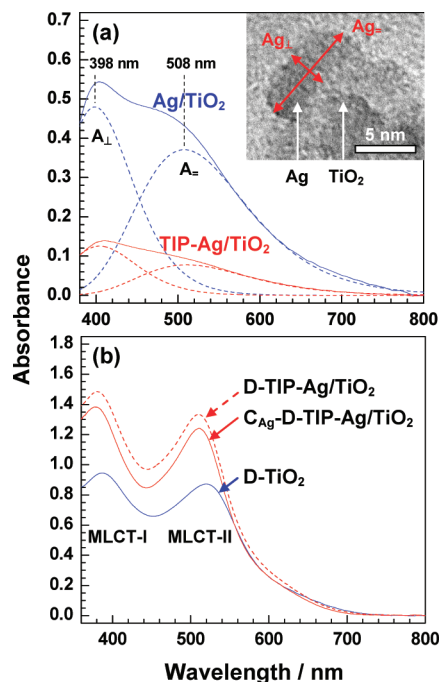


Figure 3. (a) Plasmonic absorption spectra of Ag NPs in Ag/TiO₂ (blue solid curve) and TIP-Ag/TiO₂ (red solid curve). Each spectrum was decomposed into two absorption peaks (blue or red dashed curves) depending upon the geometry of Ag NPs. The inset shows a TEM image of the side view of Ag NP on TiO₂. Ag₁ and Ag₂ indicate the direction in the geometry of Ag NP. (b) UV-vis absorption spectra of D-TiO₂ (blue solid curve), D-TIP-Ag/TiO₂ (red dashed curve), and C_{Ag}-D-TIP-Ag/TiO₂ (red solid curve).

A change in the average oxidation state of titanium in TIP-Ag/TiO₂ samples was also observed. XPS spectra in the Ti (2p) region show two peaks, assignable again to spin-orbit coupled energy states featuring $J = 3/2$ and $1/2$ (Figure 2b). In the spectrum of bare TiO₂, symmetric peaks for Ti 2p_{3/2} and Ti 2p_{1/2} appear at 458.8 and 464.5 eV, respectively. The binding energies and bandwidths of Ti (2p) in the XPS spectrum of Ag/TiO₂ are identical to those for bare TiO₂, indicating that titanium remains in oxidation state IV. For TIP-Ag/TiO₂, however, both Ti (2p) peaks in the are shifted to a lower energy region, but with higher energy tailing that again points to the presence of overlapping pairs of peaks. (See Table S1.) We denoted the deconvolved peaks at 458.8 and 464.5 eV, assignable to Ti 2p_{3/2} and Ti 2p_{1/2}, as Ti II_{3/2} and Ti II_{1/2}, respectively, and the deconvolved peaks at 458.3 and 464.0 eV, also assignable to Ti 2p_{3/2} and Ti 2p_{1/2}, as Ti I_{3/2} and Ti I_{1/2}, respectively. The binding energies of Ti II_{3/2} and Ti II_{1/2} in TIP-Ag/TiO₂ precisely match those of bare TiO₂ and indicate, therefore, the presence of Ti atoms in oxidation state IV. The significantly lower binding energies for Ti I_{3/2} and Ti I_{1/2} indicate the presence as well of partially reduced titanium atoms (i.e., atoms in an oxidation state less than IV). The reducing equivalents presumably come from metallic silver. Together with the results above for Ag, they point to the formation silver titanate compound(s)—most likely as shells around silver cores (although the only compelling evidence for core/shell structures (Figure 2c) is the subsequent stability of the putative metallic silver cores in the presence of tri-iodide). Turning again to the results above for silver, the most reasonable formulation of the titanate material is Ag_YTiO₃ (1 < Y < 2).

Photoelectrode Optical Properties. The color of Ag/TiO₂ is dark brown, while bare TiO₂ is colorless (see Figure S1). The extinction spectrum of the Ag NPs spans the range from 360 to 800 nm, with λ_{max} at 404 nm and a shoulder at ~ 500 nm (Figure 3a). The extinction spectrum can be reasonably well treated as a pair of bands that are Gaussian on energy scale and that peak at 3.11 eV (398 nm) and 2.44 eV (508 nm) (Figure 3a). Small, nonaggregated spherical particles typically yield a single peak, while elliptical and rod-shaped NPs yield pairs of bands corresponding to energetically distinct transverse and longitudinal excitation of free electrons. Link and El-Sayed, for example, observed that gold nanorods display two plasmonic bands and that the feature associated with absorption and scattering via transverse (horizontal) oscillation shifts to the red as the length of nanorod increases.³¹ Similarly, Rand and co-workers showed that 5 nm Ag NPs having an elliptical shape with an aspect ratio of ~ 2.0 exhibit a pair of plasmonic absorption bands peaking at ~ 400 and ~ 490 nm.²⁰ Based on their results, we have speculatively interpreted the observation here of a pair of bands as similarly indicating that the Ag NPs are elliptically shaped. Thus, we have tentatively assigned the higher energy peak (A_{\perp}) at 398 nm to Ag_⊥ and the lower energy peak (A_{\parallel}) at 508 nm to Ag_∥. These values point to an aspect ratio of ~ 2.6 for Ag_⊥ versus Ag_∥, as shown in the inset of Figure 3a. Consistent with the apparent similarity of aspect ratios, the difference here between peak energies for A_{\perp} and A_{\parallel} (0.67 eV) is close to that for the silver NPs described by Rand et al.²⁰

For TIP–Ag/TiO₂, the wavelengths for A_{\perp} and A_{\parallel} are red-shifted by 6 and 3 nm, respectively, compared to their values for Ag/TiO₂. Reduction in the size of the silver nanoparticles (due to conversion of their exteriors to silver titanate) should yield blue shifts. Evidently this effect is more than counter-balanced by increasing the refractive index of the local environment (i.e., silver titanate versus air (essentially vacuum)). The wavelengths of extinction maxima are well-known to be sensitive to the refractive index and the thickness of the immediate surroundings.^{12,15}

The LSPR-based extinction of TIP–Ag/TiO₂ is only about a quarter of that of Ag/TiO₂. Based on the anticipated proportionality between the metal NP extinction and volume,¹⁵ the thickness of the silver titanate shell surrounding the Ag NP is estimated to be ca. 2 nm. We observed that extending either the TIP-reflux period or the subsequent calcination time further diminished plasmonic band intensities, implying further thickening of shells at the expense of metallic cores.

Electronic absorption spectra for the well-known ruthenium-based dye, N719, adsorbed on bare TiO₂ (designated D–TiO₂) and TIP–Ag/TiO₂ (designated D–TIP–Ag/TiO₂) are shown in Figure 3b. For ease of measurement, the underlying TiO₂ samples were prepared as $\sim 6 \mu\text{m}$ thick transparent films (Figure S2). Since the extinction spectrum of D–TIP–Ag/TiO₂ includes contributions from Ag NPs, we subtracted the spectrum of TIP–Ag/TiO₂ from D–TIP–Ag/TiO₂ ($C_{\text{Ag}} - \text{D-TIP-Ag/TiO}_2$, red solid curve in Figure 3b) before comparing dye spectra. Listed in Table S2 are λ_{max} and peak absorbance values for the two metal-to-ligand charge transfer bands of N719 (MLCT-I and MLCT-II) on TiO₂ and TIP–Ag/TiO₂. In the presence of TIP-treated silver nanoparticles, the dye absorption, λ_{max} of MLCT-I was blue-shifted from 388 nm (3.20 eV) to 379 nm (3.28 eV) and that of MLCT-II was also blue-shifted from 520 nm (2.38 eV) to 511 nm (2.43 eV).

As shown in Figure 3b and Table S2, the absorbance of MLCT-II in $C_{\text{Ag}} - \text{D-TIP-Ag/TiO}_2$ (1.24) is 1.42 times higher

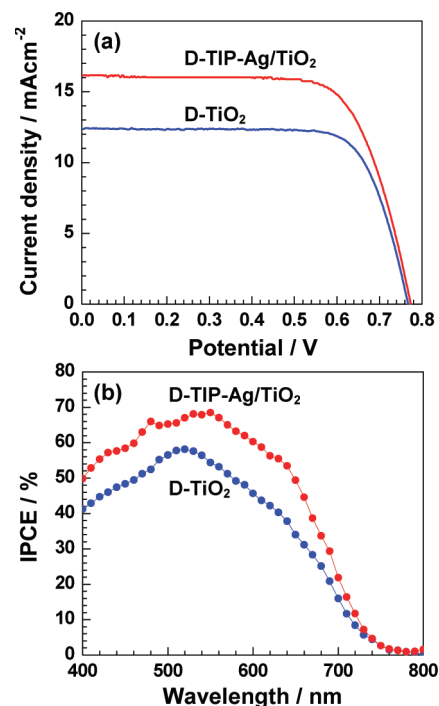


Figure 4. J – V (a) and IPCE curves (b) of D–TiO₂ and D–TIP–Ag/TiO₂ as indicated.

than that in D–TiO₂ (0.87). An increased surface area of Ag-deposited TiO₂ NPs could contribute to this increase. Thus, the number of N719 dye molecules adsorbed on $C_{\text{Ag}} - \text{D-TIP-Ag/TiO}_2$ and D–TiO₂ per square centimeter was calculated by measuring the absorbance of the detached dye in basic KOH solution. The number of dye molecules in $C_{\text{Ag}} - \text{D-TIP-Ag/TiO}_2$ was 1.18 times larger than that in D–TiO₂ (Table S2). The increased dye loading alone, however, is not sufficient to account for the increased absorbance of MLCT-II (1.42). The remaining difference (a factor of ca. 1.2) can be attributed to plasmonic amplification of the apparent extinction coefficient of the molecular light harvester.

Plasmonic Photoelectrode Behavior in DSSCs. D–TiO₂ and D–TIP–Ag/TiO₂ were prepared in forms suitable for DSSCs. Briefly, the materials consisted of supported-films featuring an $\sim 11 \mu\text{m}$ thick transparent layer, topped by an $\sim 8 \mu\text{m}$ thick light-scattering layer (Figure S2). Once assembled, the films were loaded with N719. Shown in Figure 4a are J – V curves. From the curves it is clear that while the open-circuit voltages of D–TIP–Ag/TiO₂-containing cells are similar to those of D–TiO₂-containing cells, the short-circuit photocurrent density (J_{SC}) with D–TIP–Ag/TiO₂ ($16.2 \text{ mA} \cdot \text{cm}^{-2}$) is 1.31 times higher than with D–TiO₂ ($12.4 \text{ mA} \cdot \text{cm}^{-2}$). The overall light-to-electrical energy conversion efficiencies (η) are 8.9% (with Ag) and 7.1% (without Ag), i.e., a relative efficiency increase of 25% when silver nanoparticles are included in the photoanode. (The cases shown are the best performing cells of more than 10 each, with and without silver. The corresponding average efficiency values (and error bars) are reported in Table S3, along with other cell performance parameters. The averaged data likewise show silver-containing cells to be superior to silver-free cells.) The efficiency enhancement in the presence of silver can be seen to arise chiefly from an increase in photocurrent density. Consistent with this observation, the wavelength-dependent incident-photon-to-current-efficiency

(IPCE) with D–TIP–Ag/TiO₂ is significantly higher than with D–TiO₂ across the visible spectrum (Figure 4b). The ratio of integrated IPCE values (1.27) is similar to the ratio of J_{SC} values (1.31). A reviewer has raised the question of whether silver incorporation influences the rate of electron interception by the oxidized shuttle. In principle, a decrease in interception rate could lead to an increase in photocurrent due to higher electron collection efficiency. In practice, since iodide/tri-iodide cells already approach 100% in terms of current collection efficiency, there is very little room for performance improvement via improved charge collection. Nevertheless, we performed open-circuit photovoltage decay measurements on silver-containing and silver-free DSSCs, as these measurements report on relative rates of interception. As shown in Figure S3, the decay curves are similar for the two types of cells.

Finally, while there is good agreement between the wavelength maximum in the IPCE plot (IPCE_{max}) and the dye absorption maximum, λ_{max} (=520 nm) for the D–TiO₂ system, the IPCE_{max} for the D–TIP–Ag/TiO₂ system is red-shifted by 40 nm from λ_{max} (=510 nm). This phenomenon was also observed in our previous report.¹⁷ For an organic photovoltaic cell, Rand and co-workers likewise observed a red shift in the IPCE_{max} relative to λ_{max} when Ag nanoparticles were incorporated.²⁰ In rationalizing similar behavior (i.e., red shift of IPCE_{max}) for photocells containing gold nanoparticles, Hagglund et al. focused on wavelength-dependent plasmonic enhancement of the rate of electron injection by dyes into photoanodes.¹⁹ While wavelength-dependent plasmon effects are presumably the cause of the shift in IPCE_{max} seen here, the detailed explanation likely does not involve injection behavior as the yield for electron injection from N719 into titanium dioxide is already close to unity.

CONCLUSIONS

In summary, localized surface plasmon resonance effects associated with spatially dispersed and protectively coated silver nanoparticles can be exploited to enhance the light-harvesting efficiency, the photocurrent density, and the overall light-to-electrical-energy-conversion efficiency of high-area DSSCs based on N719 and nanoparticulate TiO₂ photoanodes. Overall efficiency improvements of ca. 25% (i.e., increases in η from ~7% to ~9%) were obtained. Roughly half the improvement can be traced to increased dye loading by the photoanodes following silver incorporation, with the remaining improvement coming from LSPR enhancement of the effective absorption cross section of N719. While the findings are encouraging, we had hoped, based on our earlier work with low-area photoelectrodes,¹⁷ to observe substantially greater enhancements—especially with regard to the dye absorption cross section. Almost certainly diminishing the magnitude of the plasmonic amplification effects is loss of approximately 75% of the initially introduced metallic silver to formation of a mixed titanium/silver oxide. The loss diminishes the intensity of the localized surface plasmon resonance and, therefore, the magnitude of the electromagnetic field created by plasmon excitation. Additionally, to the extent that the mixed metal oxide exists as a shell around each metallic silver core, dye molecules are spatially separated from the plasmonic core particles and subjected, therefore, to smaller electromagnetic fields. An attractive idea for further investigation would be to find a method for protecting silver particles that yields thinner barrier coatings and that does not entail loss of metallic silver. When incorporated in photoanodes and then plasmon-excited,

these particles should subject neighboring dye molecules to much larger electromagnetic fields, resulting in substantially greater enhancement of dye absorbances and, presumably, greater efficiency improvements (provided that offsetting effects due to plasmon enhancement of the radiative decay rate of the photoexcited dye and concomitant diminution of injection yields are not important).

ASSOCIATED CONTENT

S Supporting Information. Experimental details, photographs, and SEM images. This material is available free of charge via the Internet at <http://pubs.acs.org>.

AUTHOR INFORMATION

Corresponding Author

*E-mail: j-hupp@northwestern.edu.

ACKNOWLEDGMENT

We thank Dr. Stacey Standridge for critically reading and commenting on the manuscript. SEM and XPS measurements were performed in the EPIC facility of NUANCE at Northwestern University. This material is based upon work supported as part of the ANSER Center, an Energy Frontier Research Center funded by the U.S. Department of Energy, Office of Science, Office of Basic Energy Sciences under Award Number DE-SC0001059. We also acknowledge the government of Korea for partial postdoctoral fellowship support for NCJ through the National Research Foundation of Korea (grant NRF-2009-352-D00055) and the government of Thailand's Commission on Higher Education for providing partial graduate fellowship support for CP through its program on Strategic Fellowships for Frontier Research Networks.

REFERENCES

- (1) Kay, A.; Gratzel, M. *Chem. Mater.* **2002**, *14*, 2930–2935.
- (2) Taguchi, T.; Zhang, X. T.; Sutanto, I.; Tokuhito, K.; Rao, T. N.; Watanabe, H.; Nakamori, T.; Uragami, M.; Fujishima, A. *Chem. Commun.* **2003**, 2480–2481.
- (3) Law, M.; Greene, L. E.; Johnson, J. C.; Saykally, R.; Yang, P. *Nat. Mater.* **2005**, *4*, 455–459.
- (4) Martinson, A. B. F.; Elam, J. W.; Pellin, M. J.; Hupp, J. T. *Nano Lett.* **2007**, *7*, 2183–2187.
- (5) Hamann, T. W.; Martinson, A. B. E.; Elam, J. W.; Pellin, M. J.; Hupp, J. T. *Adv. Mater.* **2008**, *20*, 1560–1564.
- (6) Lee, K.; Park, S. W.; Ko, M. J.; Kim, K.; Park, N. G. *Nat. Mater.* **2009**, *8*, 665–671.
- (7) Lee, C. Y.; Hupp, J. T. *Langmuir* **2010**, *26*, 3760–3765.
- (8) Li, T. C.; Spokoyny, A. M.; She, C. X.; Farha, O. K.; Mirkin, C. A.; Marks, T. J.; Hupp, J. T. *J. Am. Chem. Soc.* **2010**, *132*, 4580–4582.
- (9) Nattestad, A.; Mozer, A. J.; Fischer, M. K. R.; Cheng, Y. B.; Mishra, A.; Bauerle, P.; Bach, U. *Nat. Mater.* **2010**, *9*, 31–35.
- (10) Li, L.; Gibson, E. A.; Qin, P.; Boschloo, G.; Gorlov, M.; Hagfeldt, A.; Sun, L. C. *Adv. Mater.* **2010**, *22*, 1759–1762.
- (11) Nie, S.; Emory, S. R. *Science* **1997**, *275*, 1102–1106.
- (12) Jung, L. S.; Campbell, C. T.; Chinowsky, T. M.; Mar, M. N.; Yee, S. S. *Langmuir* **1998**, *14*, 5636–5648.
- (13) Brockman, J. M.; Nelson, B. P.; Corn, R. M. *Annu. Rev. Phys. Chem.* **2000**, *51*, 41–63.
- (14) Srituravanich, W.; Fang, N.; Sun, C.; Luo, Q.; Zhang, X. *Nano Lett.* **2004**, *4*, 1085–1088.
- (15) Willets, K. A.; Van Duyne, R. P. *Annu. Rev. Phys. Chem.* **2007**, *58*, 267–297.

- (16) Kelly, K. L.; Coronado, E.; Zhao, L. L.; Schatz, G. C. *J. Phys. Chem. B* **2003**, *107*, 668–677.
- (17) Standridge, S. D.; Schatz, G. C.; Hupp, J. T. *J. Am. Chem. Soc.* **2009**, *131*, 8407–8409.
- (18) Ihara, M.; Tanaka, K.; Sakaki, K.; Honma, I.; Yamada, K. *J. Phys. Chem. B* **1997**, *101*, 5153–5157.
- (19) Haggglund, C.; Zach, M.; Kasemo, B. *Appl. Phys. Lett.* **2008**, *92*, 013113.
- (20) Rand, B. P.; Peumans, P.; Forrest, S. R. *J. Appl. Phys.* **2004**, *96*, 7519–7526.
- (21) Wen, C.; Ishikawa, K.; Kishima, M.; Yamada, K. *Sol. Energy Mater. Sol. Cells* **2000**, *61*, 339–351.
- (22) Ishikawa, K.; Wen, C. J.; Yamada, K.; Okubo, T. *J. Chem. Eng. Jpn.* **2004**, *37*, 645–649.
- (23) Standridge, S. D.; Schatz, G. C.; Hupp, J. T. *Langmuir* **2009**, *25*, 2596–2600.
- (24) Lai, W. H.; Su, Y. H.; Teoh, L. G.; Hon, M. H. *J. Photochem. Photobiol., A* **2008**, *195*, 307–313.
- (25) Chou, C. S.; Yang, R. Y.; Yeh, C. K.; Lin, Y. J. *Powder Technol.* **2009**, *194*, 95–105.
- (26) Akiyama, T.; Aiba, K.; Hoashi, K.; Wang, M.; Sugawa, K.; Yamada, S. *Chem. Commun.* **2010**, *46*, 306–308.
- (27) Qi, J.; Dang, X.; Hammond, P. T.; Belcher, A. M. *ACS Nano* **2011**, *5*, 7108–7116.
- (28) Brown, M. D.; Suteewong, T.; Kumar, R. S. S.; D’Innocenzo, V.; Petrozza, A.; Lee, M. M.; Wiesner, U.; Snaith, H. J. *Nano Lett.* **2011**, *11*, 438–445.
- (29) Li, Z. Y.; Huang, H. M.; Shang, T. C.; Yang, F.; Zheng, W.; Wang, C.; Manohar, S. K. *Nanotechnology* **2006**, *17*, 917–920.
- (30) Weaver, J. F.; Hoflund, G. B. *Chem. Mater.* **1994**, *6*, 1693–1699.
- (31) Link, S.; Ei-Sayed, M. A. *Annu. Rev. Phys. Chem.* **2003**, *54*, 331–366.